



Investigation of Tie Bars Axial Force Demands in Composite Plate Shear Walls—Concrete Filled

Erkan Polat¹ · Hadi Kenarangi² · Michel Bruneau³

Received: 10 November 2020 / Accepted: 23 March 2021 / Published online: 1 April 2021
© Korean Society of Steel Construction 2021

Abstract

Tie bars axial force demands due to concrete dilation and prying action were investigated through numerical studies. In the first part of this study, the Karagozian and Case Concrete model, which proved to provide reasonable in-plane flexural cyclic inelastic wall response while accounting for concrete dilation effect, was used to investigate the variation of confinement inside the infill concrete, the distribution of passive confining pressures at the steel–concrete interface, and the resulting tie bar axial force demands. Finite element analyses involving C-PSW/CF having different tie spacings, wall depths, and wall thicknesses were performed. In the second part of this study, the influence of plate local buckling on tie bar axial force demand was investigated and explained by prying action. A separate finite element study was performed to investigate the significance of prying action and equations were developed from free-body diagrams. The results showed the significance of the passive confining pressures due to concrete dilation, and prying action due to local plate buckling, on imparting axial forces in tie bars. Neither of these behavior are currently considered as design parameters for tie bars. The numerical analyses and results presented here are intended to provide useful insights and direction for the design and instrumentation of future C-PSW/CF experiments by the broader research community.

Keywords Composite plate shear walls · Concrete-filled · Confinement · Confining pressure · Prying action · Tie bar

1 Introduction

Composite Plate Shear Wall–Concrete Filled (C-PSW/CF) consists of dual planar steel web plates having concrete infill, as defined in AISC-341 (AISC, 2016). The dual steel web plates are interconnected by tie bars. For building applications, these walls are used to provide in-plane flexural resistance to severe wind and earthquake loads. One of the roles of tie bars is to provide stability of the unit during construction, another is to provide load transfer to develop composite action of the steel plates and the infill concrete under wall deformation. Tie bars also serve to locally redistribute load

from the steel plates to the concrete infill following the steel plates local buckling (Polat & Bruneau, 2018). Tie bars can also serve other purposes in specific applications, such as in nuclear power plants when subjected to extreme thermal loads, but scope of the study here is limited to buildings having flexural walls.

While the above functions of tie bars are understood, there is no test data providing explicit tie bar axial force demands and response under inelastic in-plane flexural wall response, even though tie bars have failed in some past tests [e.g., Bhardwaj et al. (2019), Ramesh (2013)]. Existing design equations to size tie bars in C-PSW/CF are approximate and not based on models of the mechanisms that can lead to their failure in walls subjected to in-plane flexure. While these design equations are presumed to be adequate, further knowledge generated by additional experimental research will be needed to verify this. However, for this future research to be successful, guidance must be provided on possible expected causes of tie bar failures in such walls, so that specimens can be adequately instrumented to capture the behaviors leading to these failures. This paper presents findings and fundamental observations from numerical

✉ Erkan Polat
erkanpolat@munzur.edu.tr

¹ Department of Civil Engineering, Munzur University, Tunceli, Turkey

² Modjeski and Masters, Inc., 100 Sterling Parkway, Suite 302, Mechanicsburg, PA 17050, USA

³ Department of Civil, Structural and Environmental Engineering, University at Buffalo, State University of New York, 130 Ketter Hall, Buffalo, NY 14260, USA

analyses conducted to explore what may be some of these mechanisms that induce axial tie bar forces in C-PSW/CF.

The following sections summarize relevant past research and existing design provisions for tie bars in C-PSW/CF, describe the assumptions made in this analytical study, and present results from finite element analyses that have allowed to identify two mechanisms currently not considered in the design of these walls and that could impart axial force demands on tie bars, namely: (1) the effect of possible confinement pressures, and (2) the development of prying action during local buckling. Given that these two mechanisms have not been reported in the prior literature, the benefit of the numerical analyses and results presented here is to provide insights and direction for the design and instrumentation of future experiments by the broader research community. These future experiments will not only allow to verify and quantify the impact of the phenomena reported here as a basis for the development of closed-form equations to determine the axial forces to be used in the design of tie bars, but also to challenge the assumptions made in the current study.

It is important that the results presented here be understood and appreciated in that perspective, and not interpreted as predictions of absolute accuracy. The development of a complete understanding of the non-linear inelastic behavior of all components of C-PSW/CF is a complex undertaking that will require multiple iterations and studies.

2 Literature Review

2.1 Tie Bars

Tie bar failures have sporadically been reported in a few past C-PSW/CF tests, but none have been documented to the extent necessary for rigorous analysis. Ramesh (2013) reported failure of multiple tie bars in the flange of a 8115 mm (319.5 in) tall cantilever wall having a T-shape cross-section tested under cyclic loading. This flange had an infill concrete thickness of 219 mm (8.63 in), a steel plate thickness of 4.76 mm (3/16 in), and used 9.53 mm (3/8 in) diameter threaded rods as tie bars spaced at 114 mm (4.5 in) in the vertical and horizontal directions. Unfortunately, the sequence of tie failure was not documented (personal communication, Prof. Michael E. Kreger, Dept. of Civil, Construction, & Environmental Engr., University of Alabama, October 10, 2019), the tie bars were not instrumented, and their steel grade was not reported. In a separate study (Bhardwaj et al., 2019), a single tie bar failed in a wall subjected to combined in-plane and out-of-plane loading. The tie bar was instrumented in this case, but location of the strain gages along the tie bar was not provided, and the specimen failed in a complex biaxial and torsional mode; none of the analyses conducted for that wall reported the tie

bar strains at failure (Bhardwaj et al., 2019; Terranova et al. 2017, 2019).

The AISC 341-16 Seismic Provisions provide an equation to calculate the axial force demand in the tie bars of planar C-PSW/CF having cross-section with round boundary elements. This equation sums demands T_1 and T_2 , where T_1 was derived by a design analogy assuming fictitious shears corresponding to locally buckled web plates developing plastic hinges on horizontal yield lines along the tie bars and at mid-vertical distance between tie-bars (Alzeni & Bruneau, 2014), and T_2 was derived by calculating the force needed to prevent splitting of the concrete element on a plane parallel to the steel plate when compressive loading is solely applied to the concrete (Varma et al., 2014). Both T_1 and T_2 are recognized to be conservative but not representative of actual demand. New provisions for coupled C-PSW/CF (AISC 2022) provide a tie bar spacing requirement derived based on the flexibility and shear buckling of empty steel modules before concrete placement (Varma et al., 2019), as an indirect way to size tie bars, without calculating axial force demands and independent of tie bar steel grade.

Prior analytical work also focused on different related topics. For example, Zhang et al. (2014) used finite element models to investigate the effect of shear studs on the development of partial composite action in wall sections. Design recommendations have also been formulated by others for shear demands on tie bars to achieve composite action (Corus, 2003). However, these do not provide information on axial force demands on tie bars for C-PSW/CF subjected to in-plane bending.

3 Concrete Models

Some research projects have used finite element analysis for the simulation of the global force–displacement (or moment–rotation) cyclic inelastic behavior of C-PSW/CF with different aspect ratios (defined as wall height to total cross-section depth). Alzeni and Bruneau (2014) used ABAQUS (Hibbett & Sorensen, 2011) to perform finite element simulation of four experimentally tested planar C-PSW/CF with height-to-depth aspect ratio of approximately 2.5 using the Concrete Damage Plasticity (CDP) material model for the concrete. The simulations, however, were not able to capture the pinching effect observed in the cyclic testing. Polat and Bruneau (2017) used LS-Dyna (LSTC, 2013) to simulate the same experimental wall behavior. The pinching effect was successfully captured using the Winfrith model (LSTC, 2013), which can simulate the opening and closure of concrete cracking that has been shown to be responsible for the pinching effect in concrete-filled members [e.g., Imani and Bruneau (2014) and Bruneau et al. (2018)]. Epackachi et al. (2015) also used LS-Dyna to simulate the in-plane inelastic

cyclic response of C-PSW/CF with a wall aspect ratio of 1.0. Similarly, the observed pinching behavior was successfully replicated using the Winfrith model. Good agreement was reported between the experimentally obtained and the predicted values by the numerical models for the peak wall strength as well as for the reloading and unloading stiffness of the wall.

Kurt et al. (2016) used both ABAQUS and LS-Dyna to simulate in-plane inelastic cyclic behavior of C-PSW/CF with aspect ratio from 0.6 to 1.0. The Winfrith model was used in LS-Dyna analyses, while a brittle cracking material was used in ABAQUS to model concrete. Reasonable agreement of the wall strength and stiffness was reported (for both LS-Dyna and ABAQUS models) based on the comparison of pushover analyses with the experimentally measured envelope curves.

The above studies investigating response using different concrete models typically focused on numerically replicating the observed flexural hysteretic behavior of the walls. While use of the Winfrith model has proven to be more effective for this purpose, one of the criticisms of this concrete model is that it does not exhibit shear dilation under compression (Wu et al., 2012).

4 Investigation of Concrete Confinement, Passive Lateral Pressure and Tie Bar Axial Force

4.1 General

One of the mechanisms that can conceivably produce axial force demands on the tie bars is related to the shear dilation of concrete under compression. Similar to the confinement action developed in reinforced concrete columns and walls due to the restraining action created by the transverse reinforcement, the tie bars in C-PSW/CF can provide confinement action where compression is developed in the cross-section of a planar C-PSW/CF under in-plane flexure. In C-PSW/CF, this confining action is related to the restraining force that can be developed by the tie bars and steel web plates, which are related to tie bar axial rigidity and yield strength, and web plate flexural rigidity. The restraining action builds up in the form of passive lateral pressures that are related to the lateral expansion of concrete (shear dilation) under axial deformation. Therefore, to predict tie bar axial force demand through numerical solution, the passive lateral pressures and the confining action must be modeled using a concrete constitutive model capable of simulating the concrete shear dilation. Most importantly, it also requires an understanding of the 3-D flow of forces that lead to axial force demands in the tie bars. As such, it is one

of the objectives of the study reported here to investigate how confinement develops and varies within the volume of the infill concrete inside C-PSW/CF using a broadly used concrete constitutive model.

This was done by a parametric study carried out for different C-PSW/CF having different wall parameters (such as tie bar spacing, wall thickness, and wall depth) and the findings from that study were used to investigate: infill concrete confinement between the sandwiching plates of the wall (inside the volume of the infill concrete considering axial stress variation); passive lateral pressure distribution at the steel–concrete interface (considering interface nodal forces), and; resulting tie bar axial force demands (accounting also for the influence of steel plate local buckling).

4.2 Selection of Concrete Model

A preliminary study was first conducted to select a concrete model able to provide an acceptable representation of global wall response (i.e., in terms of cyclic stiffness and strength) while allowing the concrete dilation needed to provide reasonable tie forces. For this purpose, the previously developed and benchmarked finite element wall model that used the Winfrith model to capture global in-plane flexural wall response [developed by Polat and Bruneau (2017)] was re-used, but considering two other concrete models that include dilation effects, namely the Karagozian and Case Concrete (KCC) and Continues Surface Cap Model (CSCM) models (available in LS-Dyna). Evidently, because both the KCC and CSCM models can simulate shear dilation, results for both models show compression axial stress distributions that varied through the thickness of the infill concrete (contrary to the results for Winfrith model, which has no shear dilation). However, while both the KCC and CSCM models could not simulate the pinching experimentally observed in the inelastic hysteretic flexural behavior of the walls, results from the wall using KCC model was better in agreement with the actual wall response. Furthermore, the prediction of wall strength by the KCC model was almost the same as that from the benchmarked model (and of the actual wall), while it was overpredicted by the CSCM model. With respect to axial stress distribution along the cross-section, compression depth obtained with KCC model was found to be in better agreement than that obtained with the Winfrith and CSCM models. Based on the above findings from the preliminary study, the KCC model was chosen to investigate concrete confinement, passive lateral pressure, and tie bar axial force demand for the current parametric study considering different C-PSW/CF. More details on this preliminary study and on reasons that supported the selection of the KCC model for this study are provided in Appendix 1.

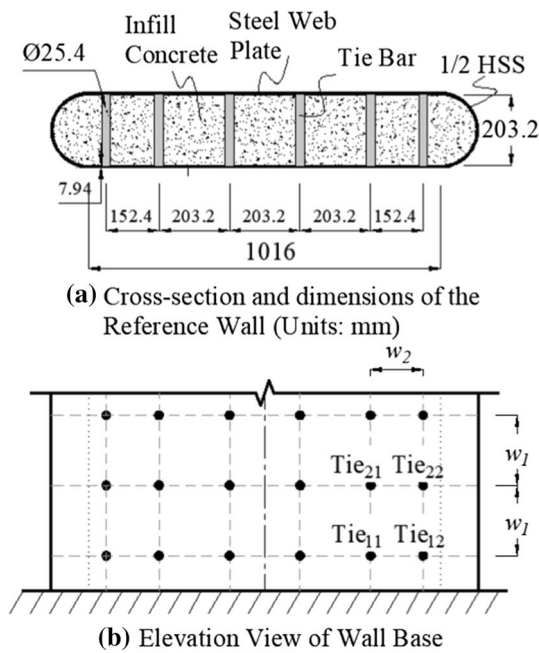


Fig. 1 Reference C-PSW/CF: **a** plan view, and; **b** elevation view of the wall base

4.3 Description of Walls

As a reference starting point, the walls used in this study to investigate tie bar axial force during in-plane flexure were modified versions of the C-PSW/CF wall with boundary elements tested by Alzeni and Bruneau (2017) under cyclic in-plane bending. Figure 1a shows the plan view and dimensions of the wall cross-section, and Fig. 1b shows the elevation view of the wall base. The boundary elements of the wall consisted of half-circular hollow structural sections (half-HSS 8.625 × 0.322) that have a diameter of 219 mm (8.625 in) and a thickness of 8.18 mm (0.322 in). The wall skin consisted of steel plates with a thickness of 7.94 mm (5/16 in) and a width of 1016 mm (40 in). The steel web plates were interconnected by tie bars (welded to the steel plates) with a diameter of 25.4 mm (1 in). The vertical and horizontal spacing between adjacent tie bars were 203 mm (8 in), except that horizontal spacing was 152 mm (6 in) between the last tie bars close to wall edge. The wall was a cantilever with a height of 3048 mm (120 in). The concrete used was self-consolidating concrete and had a uniaxial compressive strength of 48 MPa (6.9 ksi) (obtained from concrete cylinder tests), the steel web plate had a yield strength of 427 MPa (62 ksi) and the steel HSS had a yield strength of 317 MPa (46 ksi). Note that no test data were available for tie bars. Their yield strength was assumed to be 345 MPa (50 ksi). Further details on material properties and a representative stress–strain curve for steel are reported in Alzeni and Bruneau (2017). Note that

a group of four tie bars is identified in Fig. 1b. These are denoted as T_{11} , T_{12} , for the first tie bar level, and T_{21} , T_{22} for the second tie bar level. Axial force demands will be monitored in these found tie bars in the parametric study.

However, for the purpose of the present parametric study, the above wall could not be used as-is, because its boundary elements work together with the tie bars to resist the confinement pressure, which would make it impossible to generalize results—for example, in wider walls, tie bars in the flexural compression block would be further away from the boundary elements. Therefore, the model shown in Fig. 1a, was modified to not have boundary elements, as shown in Fig. 2. The wall model shown in Fig. 2a has the same dimensions as the web of the reference wall (i.e., it is the reference wall without its boundary elements). Two variations of this model were developed to investigate the effect of changing the horizontal and vertical spacing of the tie bars, the thickness of the infill concrete, and the wall depth, on the results. These models are referred to as Models A, B, and C, as illustrated in Fig. 2a–c. As shown in Fig. 2a, Model A has the same dimensions as the benchmarked model; Models B (Fig. 2b) and C (Fig. 2c) have tie bar spacing of $w_1 = w_2 = 305$ mm (12 in), which is 150% more than Model A; Model B also has a concrete thickness of $t_c = 254$ mm (10 in) instead of 203 mm (8 in), and Model C has a larger wall depth equal to 1422 mm (56 in) instead of 1016 mm (40 in). The steel and concrete material properties were kept the same in all cases.

In addition to the above three models, a variation of Model A was developed to investigate the influence of steel plate local buckling (by explicitly preventing the steel plate from buckling) on concrete confinement, confining

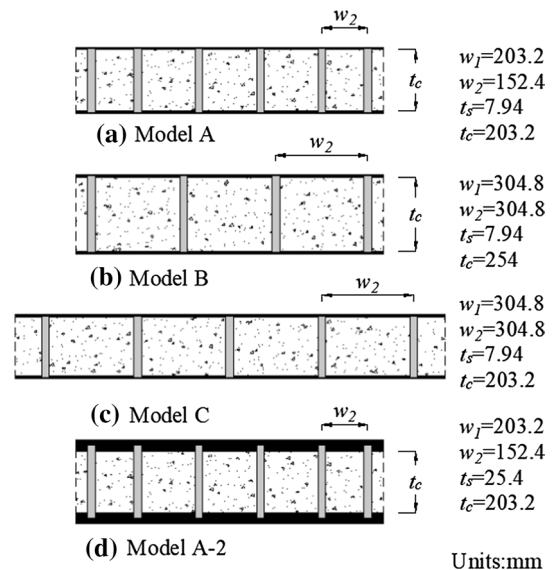


Fig. 2 Cross-section of wall models used in the parametric study: **a** Model A; **b** Model B; **c** Model C, and; **d** Model A-2

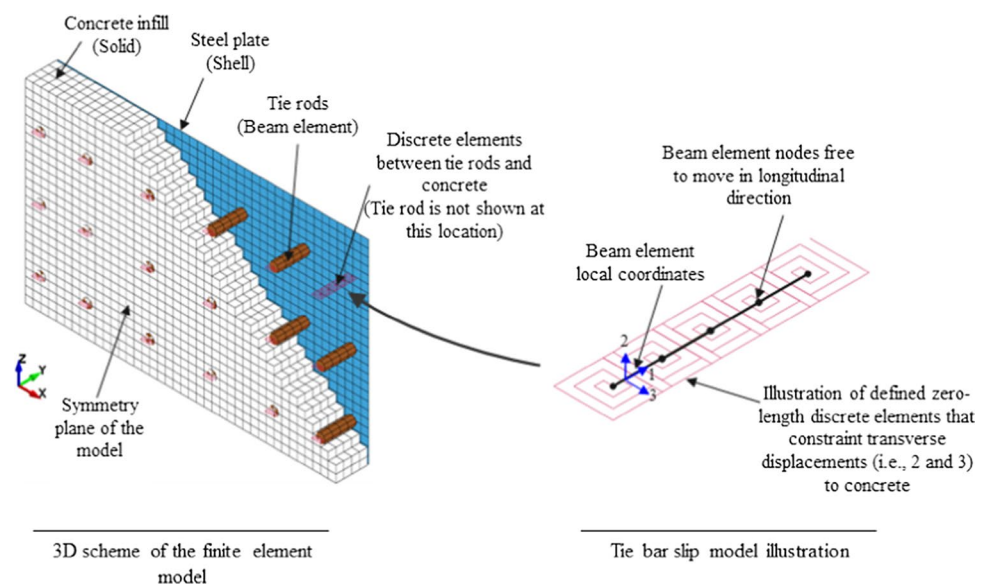
pressures, and tie bar axial force demand in absence of prying action (the effect of prying action is addressed in Section 2). As shown in Fig. 2d this model is referred to Model A-2 and has thicker steel web plates equal to 25.4 mm (1 in) instead of 7.94 mm (5/16 in) to prevent the steel plate from local buckling. For that model, beyond increasing the plate thickness, the yield strength and elastic modulus of the steel material model were adjusted so that the global lateral stiffness and strength of the wall model was not different than that for Model A. For example, the yield strength of the Model A-2 is obtained from $F_{ypl}t_{s1}/t_{s2} = 134 \text{ MPa}(19.4 \text{ ksi})$, and the elastic modulus is obtained from $(t_{s1}/t_{s2})E_s = 62487 \text{ MPa}(9063 \text{ ksi})$, where, F_{ypl} , E_s , and t_{s1} are, respectively, the plate yield strength, elastic modulus and plate thickness of Model A, and; t_{s2} is the plate thickness of Model A-2.

4.4 Tie Bar Slip Model in Finite Element Modeling

The numerical study conducted here used the previously developed finite element modeling and analysis procedures by Polat and Bruneau (2017). Complete details of this model are not repeated here due to space constraints, but some key aspects of the material models used are presented in Appendix 1. However, for the current study, a different approach was adopted for tie bar modeling, referred to as the tie bar slip model, as explained below. In the previous model, tie bars were modeled with beam elements having the same length as the solid elements of the concrete and tie bar nodes were coupled with the solid nodes of the concrete in three directions so that the slip of the tie bar elements was constrained by the concrete elements (see Appendix 1 for details of the numerical models developed using LS-Dyna). (Note that composite action in C-PSW/CF is achieved by

the shear transfer between the concrete and steel, which is in part coming through the tie bars and therefore necessitates the use of beam elements for modeling of the tie bars, rather than truss elements that do not have shear stiffness.) Here, instead, tie bar (beam element) nodes were coupled with the solid element nodes of the concrete in the two orthogonal direction transverse to the bar with no coupling in the longitudinal direction of the bar, to allow longitudinal bar slippage inside the concrete. Zero length rigid links were used in the two transverse orthogonal direction to achieve the coupling. Figure 3 shows an illustration of tie bar slip model. Note that tie bar elements are terminated at the surface of concrete and do not continue to the steel plate shell element. Therefore, to connect the tie bar end to the steel plate shell element, it is necessary to use a constraint that can transfer forces from tie bar end to the steel plate. One simple way is to use the Spotweld constraint with no failure limit. At the steel plate-concrete interface, the *constrained_spotweld* option was used to connect the beam element end nodes to shell element nodes of the web plate (note that the web plates, as shell elements, do not have a visible thickness; consequently, there is a gap equal to half the plate thickness at the steel plate-concrete interface because the shell elements are located at their mid-thickness (a default and suggested setting for modeling shell elements in LS-Dyna). Although there is a visible gap, the shell thickness is accounted in the contact simulation of the steel web plate and concrete in the analysis). This *spotweld* constraint creates a rigid beam that transmits moments, shear and normal forces. Note that the *spotweld* constraint was defined as full-strength and no failure limit state was defined. The above modeling approach did not include adhesion and friction bond between tie bars and the infill concrete, which results in unrestrained slip of the tie bars inside the concrete. Tie bar

Fig. 3 Illustration of tie bar slip model



axial force demand obtained with this slip model is constant over the entire tie bar length. This was done for simplicity, as warranted within the stated objectives for this paper.

4.5 Investigation of Confinement Through Axial Stress Variation in Concrete

The modified wall models shown in Fig. 2 were used to investigate the variation of axial stresses through the thickness of the infill concrete. The variation of confinement of the infill concrete can be inferred from the variation of axial stresses; when the lateral expansion of concrete is prevented, the axial strength of the confined concrete can exceed its uniaxial unconfined compressive capacity. For the typical planar C-PSW/CF shown in Fig. 2, the effect of confinement varies through the thickness of the infill concrete. When the infill concrete is modeled by layers of solid elements across the wall thickness, as done here, each layer exhibits different level of confinement.

For each model shown in Fig. 2, a pushover analysis was performed, and axial stresses were obtained in each layer of the infill concrete. Figures 4 and 5 show the axial stress distribution at the: (a) outermost, and; (b) innermost concrete layers of a wall region limited to half the wall depth [for clarity of labeling the figure, the results over the wall

half depth (508 mm–20 in) are only presented up to 500 mm (19.7 in) in these figures] and a height of 500 mm (19.7 in) from the wall base; obtained for Models A and C, respectively. Axial stress distribution obtained for Models B and A-2 are not included here due to space constraints. As shown in Fig. 4a, concrete axial stresses (and thus confinement) peaks at tie bar locations on the outermost layer of the infill concrete where restraining forces are locally developed. These restraining forces counteract the lateral expansion of the confined concrete. In between the tie locations, axial stresses vary in a parabolic fashion both vertically and horizontally, spanning from tie bar to tie bar. Note that, for this model, local buckling occurs between the first and second rows of tie bars. Incidentally, a more subtle occurrence of local buckling also developed between the second and third rows of tie bars, and similar variation in concrete forces is also visible there. As shown in Fig. 4b, axial stresses peak towards the center of the group of tie bars in the innermost layer of the infill concrete. Although a figure for Model B is not provided, axial stresses peaked at the two vertical tie bar locations closest to the wall edge. As shown in Fig. 5 for Model C, which has larger wall depth, variation of the axial stresses in the outermost and innermost layers are similar to Model A (Fig. 4), except that peaks are bigger due to the increased tie bar spacing. Although a figure for Model A-2 is

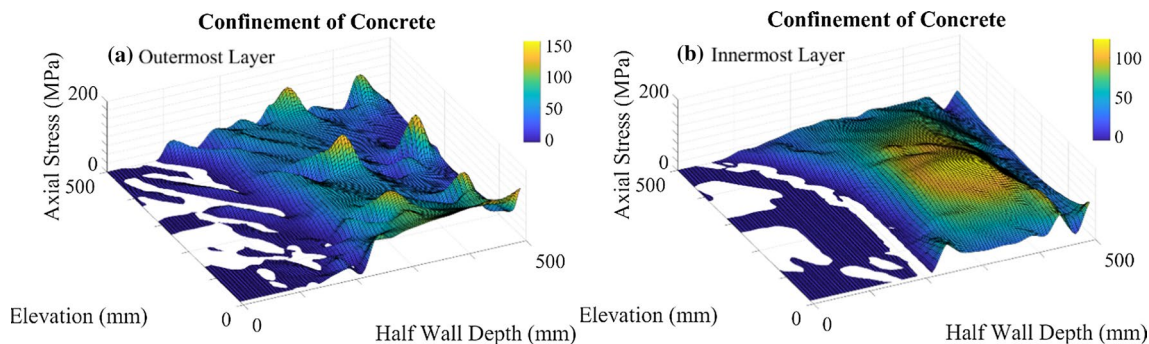


Fig. 4 Axial stress distribution in infill concrete for Model A at 4% drift ratio in the: **a** outermost layer, and; **b** innermost layer

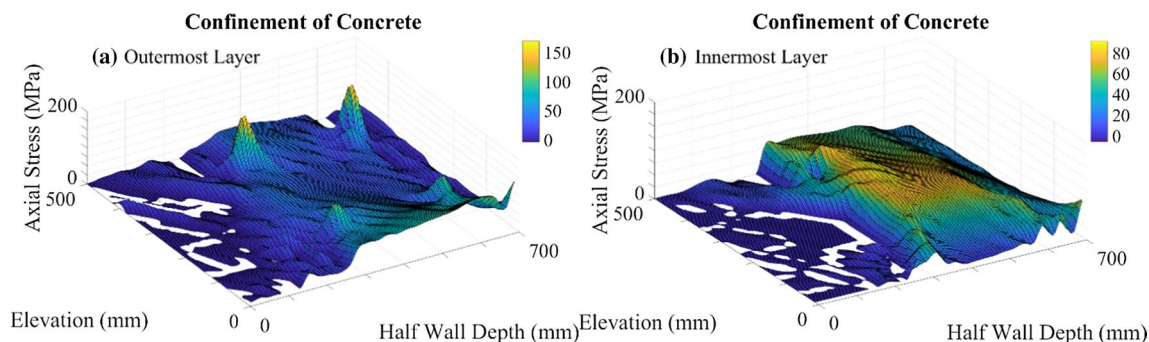


Fig. 5 Axial stress distribution in infill concrete for Model C at 4% drift ratio in the: **a** outermost layer, and; **b** innermost layer

not provided due to space constraints, variation of concrete axial stresses (and thus confinement) between the tie bar levels were similar to the results obtained for Model A with subtle changes (e.g., less acute stress peaks and smoother stress variation). The fact that the stresses were more uniformly distributed in that case is attributed to the fact that Model A-2 has thicker plates and exhibits no plate local buckling. In this case, the peak values of the stress distribution in the outermost layer are lower whereas stress values in between tie bar levels are higher.

While the above figures illustrate how concrete stress varied across the walls' depth, length, and thickness, the same results as in Figs. 4 and 5 are plotted in Figs. 6 and 7 to facilitate reading of the numerical values between the horizontal and vertical adjacent tie bars in the outermost layer. More importantly, results also illustrate how these stresses progressively change upon larger drifts, up to the 4% drift value for which results are shown in Figs. 4 and 5. Figs. 6a and 7a show the stress distribution at two wall elevations, namely at the second tie bar elevation (at 305 mm (12 in) for

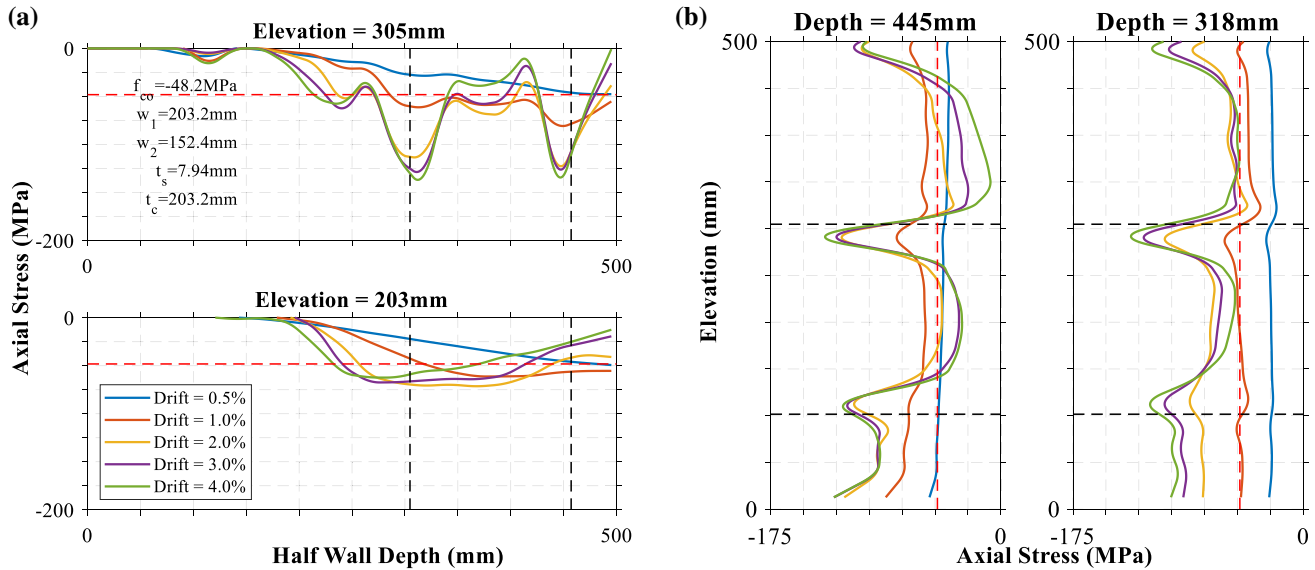


Fig. 6 Axial stress distribution in outermost layer of infill concrete for Model A at: a elevations=203 mm and 305 mm, and; b depths=318 mm and 445 mm

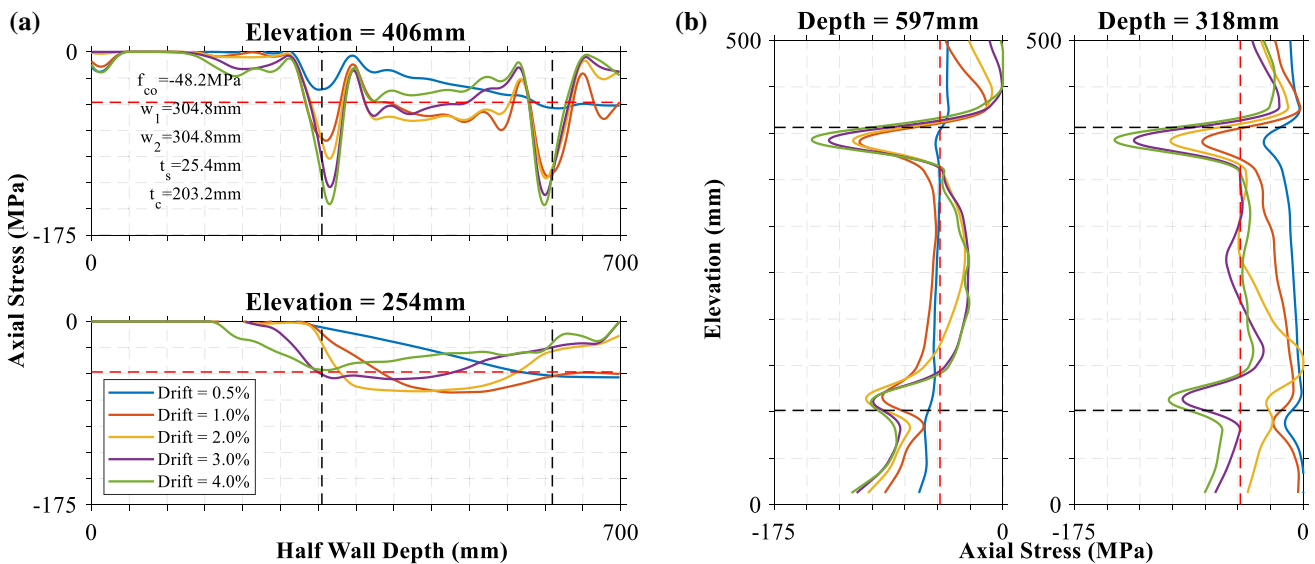


Fig. 7 Axial stress distribution in outermost layer of infill concrete for Model C at: a elevations=203 mm and 406 mm, and; b depths=318 mm and 597 mm

Model A, and; at 406 mm (16 in) for Model C) and at mid-height of the first two tie bar elevation (at 203 mm (8 in) for Model A, and; at 254 mm (10 in) for Model C). Figs. 6b and 7b show the stress distribution at two wall depth locations from the wall centerline, namely at the outermost location of tie bars (at 445 mm (17.5 in) for Model A, and; 597 mm (23.5 in) for Model C) and at mid-length of the two tie bar locations (at 318 mm (12.5 in) for Models A and C). The location of tie bars and the unconfined compressive strength of the concrete [9.69 ksi (48 MPa)] are shown by dashed lines.

Results show that, at larger drifts, confinement is increased at tie bar locations while it is reduced between the tie bar levels. For example, considering the outermost layer of the infill concrete thickness of Model A shown in Fig. 6b, the monitored concrete strength reduces below the actual compressive strength level at mid-height between the vertical tie bar levels, starting at the 2% drift ratio, and eventually becomes ineffective at the larger drifts. Similar behavior was particularly visible for Model B between the vertical tie bar levels (figure not included here). As shown in Fig. 7, the axial stress distribution for Model C is close to that shown for Model A. Axial stress distribution in these figures between the vertical tie bar levels also indicates that concrete is not effectively confined at over approximately 50% to 70% of w_f . This value is closer to 50% for smaller tie bar spacing (e.g., Model A) and closer to 70% for larger tie bar spacing (e.g., Models B and C). In other words, because of the larger tie bar spacing used for Models B and C compared to Model A, larger part of the concrete core becomes less effective at the mid distance between the tie bars and resists lower compression stresses. For Model A-2, in absence of plate local buckling, the peaks at the tie bar locations are lower compared to Model A, and the stress variation between tie bar levels is less severe and smoother.

4.6 Investigation of Passive Lateral Pressure Through Interface Nodal Forces

The variation of the concrete axial stresses reported in the previous section within the vicinity of a group of tie bars can also be shown to be related to the passive confining pressure created as a result of concrete lateral expansion at the steel plate—concrete interface. This was done here by using the interface reaction forces at the nodes of the mesh as a proxy for passive confining pressures (by equilibrium, the nodal reaction forces are the result of contact interface forces and pressures). These forces were obtained for the wall models shown in Fig. 2. The history of the interface nodal forces in the normal direction was obtained from the pushover analyses performed and plotted over the surface area of the steel plate at 4% drift ratio. Figure 8a, b shows the distribution of the passive confining pressure for Models A and C for a region covering half the wall depth and a height of 500 mm (20 in) from the wall base (results for Models B and A-2 are not included here due to space constraints). As shown, the envelopes of confining pressures are conical shapes having peaks values at the tie locations and near-zero values between the tie bar levels. For Model A-2, the confining pressure variation is smoother and reaches lower values at the tie bar levels). The magnitude of these resulting forces is significant and drives the development of axial forces in tie bars.

The interface pressure distribution shown in Fig. 8 is numerically shown in Figs. 9 and 10 at the horizontal and vertical tie bar locations for Models A and C, respectively. These figures show how nodal forces corresponding to interface pressures progressively change upon larger drifts, up to the 4% drift value considered here. The pressure distribution shown are close to triangular shape for the reported drift levels, which is logical since these plots are actually 2-D slices of the conical shapes shown in Fig. 8. Figs. 9 and 10 show that the base of these cones consistently has a base diameter of about 100 mm (4 in), regardless of the wall model and tie bar location. The peaks of the pressure distribution vary

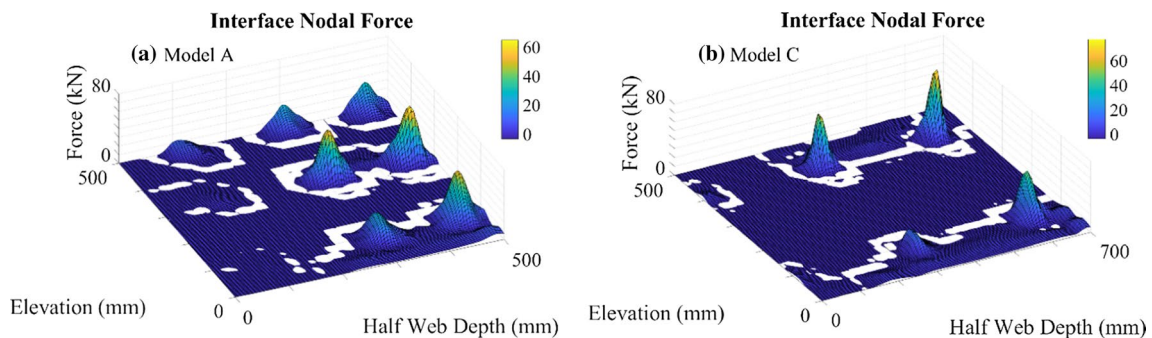


Fig. 8 Interface nodal force distribution at 4% drift ratio for: **a** Model A, and; **b** Model C

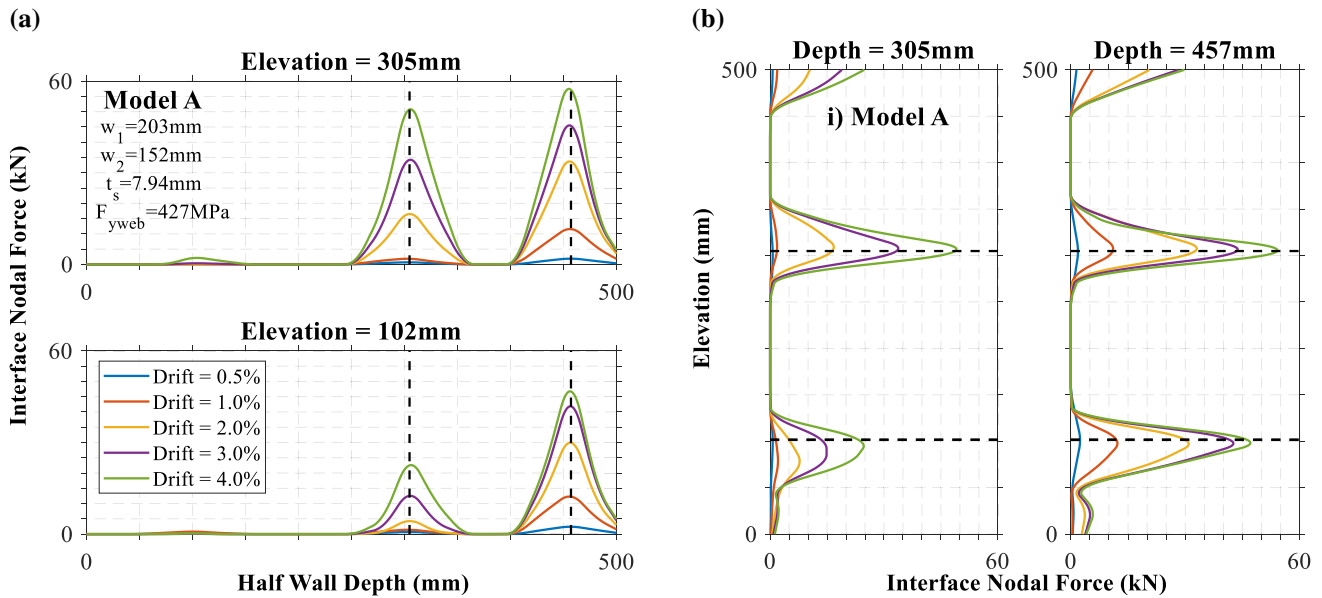


Fig. 9 Interface nodal force distribution at selected tie bar locations for Model A: at: a elevations=102 mm and 305 mm, and; b depths=305 mm and 457 mm

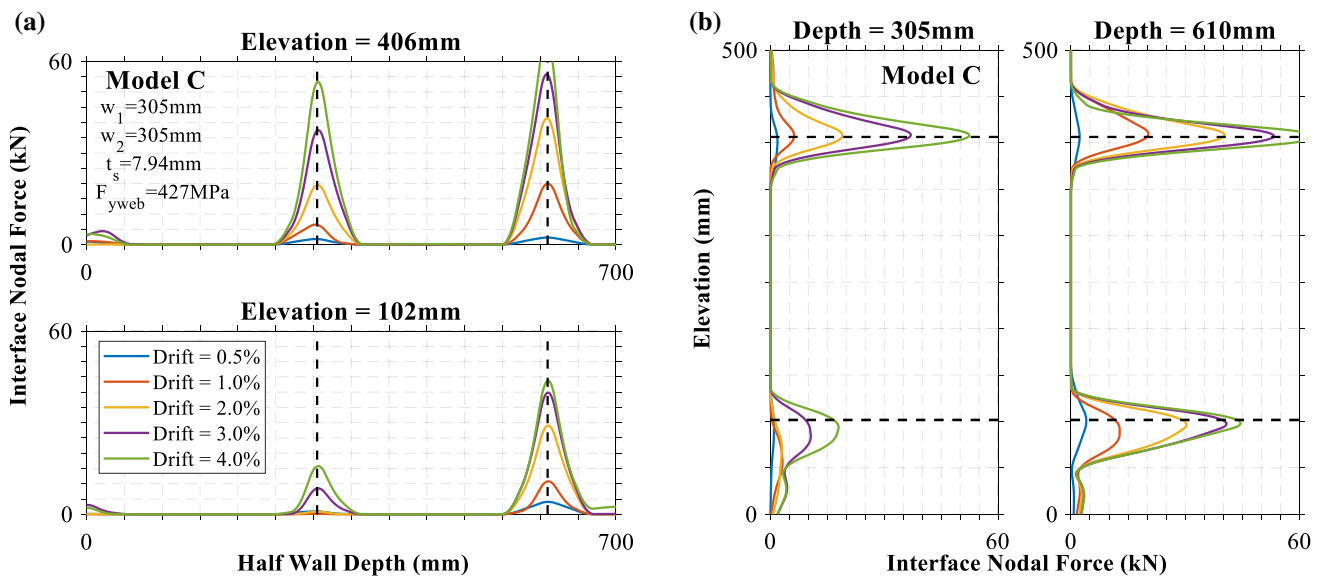


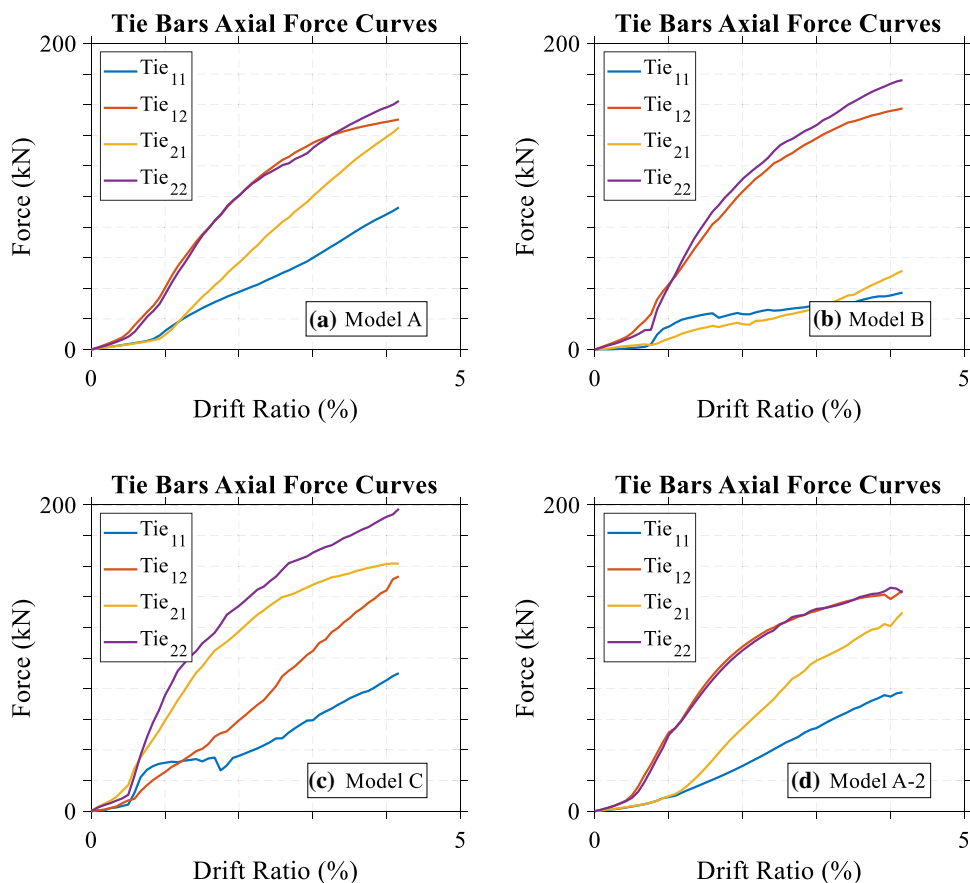
Fig. 10 Interface nodal force distribution at selected tie bar locations for Model C: at: a elevations=102 mm and 406 mm, and; b depths=305 mm and 610 mm

depending on the location of the tie bars and the peak of the pressure distribution is related to axial strain demand at the region where the tie bar is located. Note that, as discussed and shown in Fig. 3 in the finite element modeling, the tie bars were modeled as line elements and the 3-D geometry of the bars were not explicitly modeled. Modeling the bars with solid elements to capture their actual diameter might increase the diameter of the conical pressure distribution reported here for a 25.4 mm (1 in) tie bar.

4.7 Investigation of Tie Bar Axial Force Demand due to Confinement

The interface nodal forces shown in Figs. 9 and 10 were created by the axial force developed in the tie bars to resist concrete lateral expansion. Figure 11a–d shows the axial force history of the tie bars for the wall models considered for increasing drift ratios. For all the wall models considered, peak force demands occurred in the exterior tie bars,

Fig. 11 Tie bars axial force histories: **a** Model A; **b** Model B; **c** Model C; **d** Model A-2



namely Tie_{12} and Tie_{22} defined in Fig. 1b. For Tie_{22} , the axial force at 4% drift ratio, is: 158 kN (35.5 kips), 174 kN (39 kips), 192 kN (43.2 kips), and 143 kN (32 kips) for Models A, B, C, and A-2, respectively. This compares with an expected tie bar capacity of 174.2 kN (39.3 kips) for a 25.4 mm (1 in) diameter bar having a yield strength of 345 MPa (50 ksi). Note that these values would be less at lesser drift and, most importantly at lesser axial strains in the walls. Incidentally, most C-PSW/CF walls tested in the past have developed fracture of the steel plates at lower drifts than 4% [e.g. Ramesh (2013); Alzeni and Bruneau (2017)]. Fracture has been neglected in the above finite analysis models, but would eventually need to be taken into account when comparing axial demands in tie bars in experiments.

The larger force values obtained with Models B and C are attributed to the larger tie bar spacings in these walls ($w_1 = w_2 = 305$ mm (12 in)) compared to the spacing of $w_1 = 203$ mm (8 in), $w_2 = 152$ mm (6 in) in Models A and A-2. On the other hand, the larger force value in Model A compared to Model A-2 is attributed to influence of plate local buckling, which is absent in Model A-2. Note that, for Tie_{22} , there is a 15 kN (3.37 kips) difference in the force obtained with Models A and A-2. The contribution

of the plate local buckling to tie bar axial force demand can be explained by a prying action mechanism which is described in the following section. In that section, a separate numerical study is also carried out to study the development of this prying mechanism and its impact on the resulting tie bar axial forces.

5 Tie Bar Axial Force Demand Due to Prying Action

5.1 General

A second mechanism that can produce large tie bar axial forces is the prying action effect that develops during local buckling of the steel plates in the compressive regions of the cross-section during wall flexure. It is currently unknown if the tie bar axial forces developed by prying action are significant. This is investigated below, first by developing some equilibrium equations to explain the phenomena, and then using finite element analysis to illustrate the potential influence and significance of the plate thickness and tie bar diameter on tie bar axial force demands due to prying action. In the results presented below, the

magnitude of prying forces is compared to those obtained previously due to confinement effects, to assess their relative significance.

5.2 Free-Body Diagrams

In a typical planar C-PSW/CF subjected to in-plane flexure, plate local buckling will develop at some point under flexural wall deformation. For a well-designed C-PSW/CF, this will occur only after development of the plastic moment of the wall. The buckling wave typically starts to form between the tie bars at the location of the maximum moment, and more significantly in the regions of larger flexural compressive strains near the edge of the wall. Note that for a typical planar wall, the buckling wave is not uniform in amplitude but varies along the length of the wall in a three-dimensional fashion. For simplicity here, these variations of the buckling wave along the length of the wall are neglected, assuming a uniform amplitude for the buckling wave instead.

Figure 12a, b schematically illustrates how the local buckling mechanism could induce forces in the tie bars by prying action. Assuming yield lines along the horizontal lines of tie bars, focus here is on a tributary length of steel plate equal to the horizontal spacing between tie bars (Fig. 12a). Figure 12b schematically shows free-body diagrams of: (i) the equilibrium of forces within the buckled zone between two horizontal rows of tie bars, and; (ii) the equilibrium of forces due to the prying action mechanism that develops adjacent to that zone. Due to the presence of a plastic flexural moment along the yield line, the second free-body diagram shows that moment equilibrium about point A is achieved by the

moment created in the tie bar, the force couple created by the force in the tie bar (T_1) and the resultant force of the bearing pressures on the concrete (Q_{max}), and the moment in the plastic hinge (Fig. 12b). Note that a secondary moment ($P\Delta_1$) is also created due to the eccentricity, Δ_1 , between the top and bottom axial forces shown in that figure and considered in the moment equilibrium. Assuming an equivalent resultant force, Q_{max} , acting at the center of the pressure distribution, the tie bar force, T_1 , per horizontal force equilibrium, is acting in equal and opposite direction to the bearing pressure resultant ($T_1 = Q_{max}$). The prying length, L_{pr} , is given by the distance between these two forces. The prying tie force, T_1 , can be expressed by the following equation;

$$T_1 = \frac{M_p - M_{tie} + P\Delta_1}{L_{pr}} \tag{1}$$

where M_p is the plastic moment of the steel plate, M_{tie} is the moment demand in the tie bar and P is the axial force demand in the steel plate. Note that for well-proportioned walls, the contribution of the tie bar moment and secondary moment is small and can be ignored compared to the out-of-plane plastic moment of the steel plate. For example, for a tie bar diameter of 12.7 mm (0.5 in), plate thickness of 8 mm (5/16 in), and a corresponding maximum tie bar spacing of 203 mm (8 in.), results from analysis gave a contribution of the tie bar moment $M_{tie} \approx 113$ kN mm (1 kip in) and a secondary moment $P\Delta_1 \approx 181$ kN mm (1.6 kip-in), both smaller than the value of the out-of-plane plastic moment of the steel plate [$M_p \approx 1356$ kN mm (12 kip in)]. Therefore; Eq. (1) can be simplified to:

$$T_1 = \frac{M_p}{L_{pr}} \tag{2}$$

Note that the plastic moment should actually be reduced to account for vertical axial force also acting in the plate, but conservative results are obtained neglecting this effect. Per simple plastic theory, for the yielding strength of the plate, F_{yweb} , and thickness, t , the plastic moment is:

$$M_p = F_{yweb} \frac{w_2 t^2}{4} \tag{3}$$

Note that, for a typical planar C-PSW/CF, during local buckling of the plate, the prying action effect develops concurrently with the confinement action mentioned earlier and, as a result, in finite element analyses, values of the bearing pressures that develop at the steel–concrete interface include components from both the prying mechanism and the confining pressure. This makes it challenging to identify the relative contribution due to each factor, such as to quantify the prying force due to the mechanism described

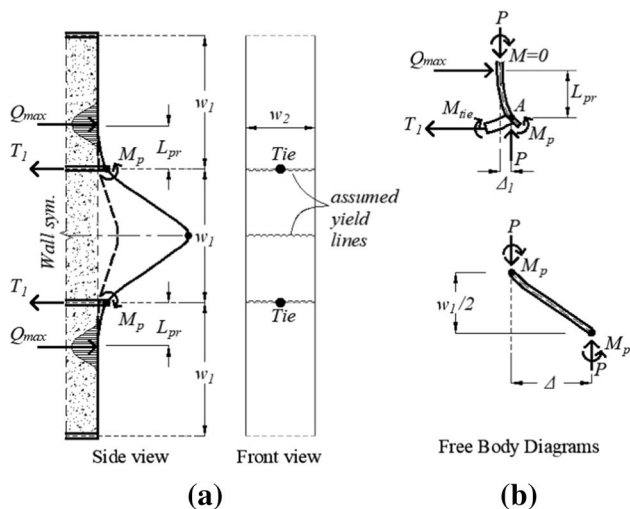


Fig. 12 Development of prying action: a local buckling on segment of wall considered, and; b free body diagrams

above excluding the influence of the concurrent confining pressures. In other words, in the case where there is also confining pressure acting concurrently, the bearing pressure shown in Fig. 12a adds up to the confining pressure, which results in a larger force resultant possibly acting at a different location. A different model is therefore needed to be able to isolate the effect of prying action using finite element analysis. In the following section, the development of prying action is investigated using such a model.

5.3 Numerical Studies

In this section, tie bar axial force demand that develop due to prying action of the steel plate undergoing local buckling is investigated. A parametric study was carried out to investigate the significance of the prying mechanism following steel plate local buckling, assuming no confining pressures can develop in the concrete. This was achieved by constraining the concrete lateral expansion in the model, as described below. Also, to simplify the analysis and allow to better identify forces developing due to prying action without having to contend with variations of the amplitude of plate local buckling along the length of the wall, analysis of a wall under pure compression was performed (i.e., to obtain uniform amplitude of the buckling wave and plastic moment along the length of the wall). Moreover, to increase computational efficiency, a partial wall was considered.

Figure 13 shows the geometry and dimensions of the partial wall in: (a) a cross-section view, and; (b) an elevation view. The model consists of three tie bars along a total height of 610 mm (24 in) with vertical tie bar spacing of $w_1 = 203$ mm (8 in)—effectively corresponding to the tributary area of one bar in an actual wall. Symmetry boundary conditions were applied to the sides of the model to simulate continuity along the wall depth with a tributary length equal to a horizontal tie bar spacing of $w_2 = 203$ mm (8 in). The infill concrete has a thickness of $t_c = 203$ mm (8 in) but symmetry boundary conditions were used for the numerical model at

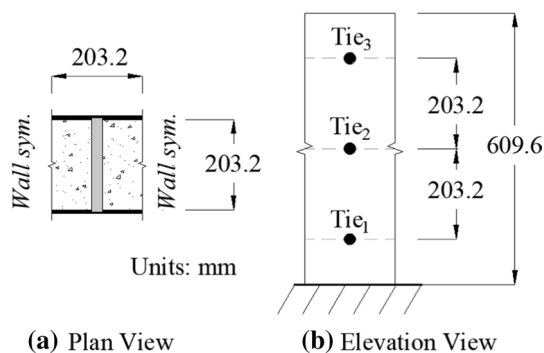


Fig. 13 Partial wall used for investigation of prying forces: **a** plan, and; **b** elevation

mid-thickness, resulting in a 102 mm (4 in) thick model. For the numerical model, the same material and element types previously described were used for the steel and concrete [$F_{yweb} = 427$ MPa (62 ksi), $f'_c = 48$ MPa (7 ksi)] and tie bars were assumed to remain elastic. The element mesh from previous studies was refined here by reducing the width of each element in half [i.e., shell elements here are 12.7×12.7 mm (0.5×0.5 in) and the solid elements are $12.7 \times 12.7 \times 12.7$ mm ($0.5 \times 0.5 \times 0.5$ in)]. The reason for using a more refined mesh was to obtain more nodal force output from the steel–concrete interface nodes, to allow plotting prying action forces more precisely without numerical smoothing. Tie bars were modeled using the tie bar slip model described earlier.

The lateral expansion of the concrete in the finite element model was prevented by fixing each of the concrete interface (concrete–steel plate) nodes in the normal direction. As part of the parametric study, cases for plates with different thicknesses were considered, namely 4.76 mm (3/16 in), 7.94 mm (5/16 in), 12.7 mm (1/2 in), and 15.88 mm (5/8 in). Furthermore, different tie bar diameters (ϕ) were considered, namely: $\phi = 6.35$ mm (0.25 in), 12.7 mm (0.5 in), and 19.05 mm (0.75 in). The model was subjected to axial deformations at the top in the form of a displacement applied on both the concrete and steel plate nodes. Figure 14 shows the finite element model developed in LS-Dyna and the von-Mises stress contours of the plate at peak deformation.

Figure 15a–d shows the resulting bearing nodal force distributions for a partial elevation of the wall (i.e., approximately between the second and third tie bar elevation) for the case having $\phi = 12.7$ mm (1/2 in) tie bars and

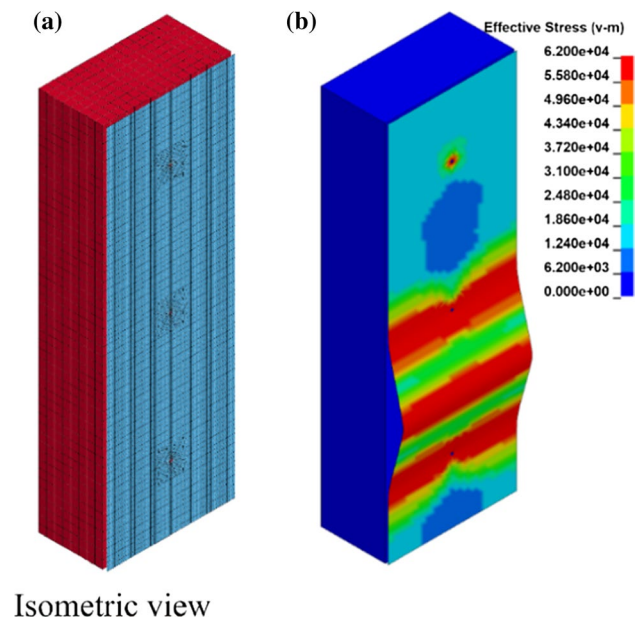


Fig. 14 LS-Dyna model for prying action investigation: **a** undeformed shape, and **b** von-Mises stress contours in deformed shape

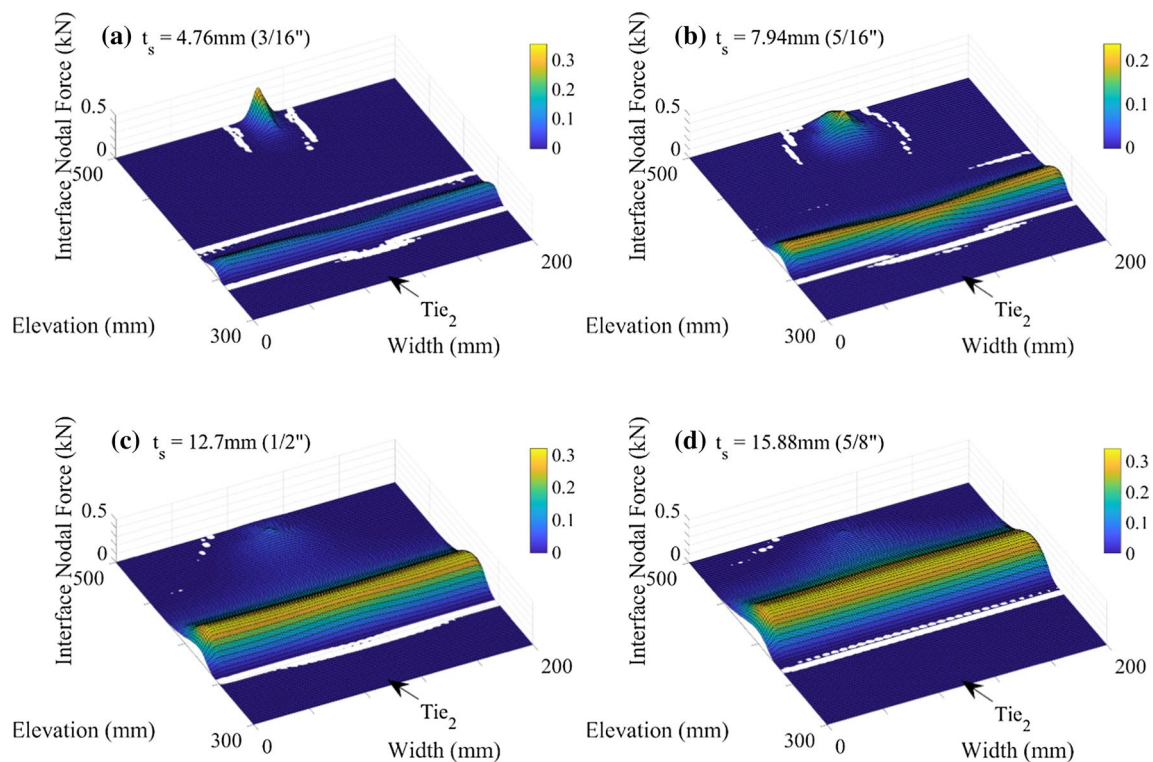


Fig. 15 Distribution of bearing pressure due to prying action after the development of plastic moment, considering plate thicknesses of: **a** 4.76 mm (3/16 in); **b** 7.94 mm (5/16 in); **c** 12.7 mm (1/2 in), and; **d** 15.88 mm (5/8 in)

the four plate thicknesses considered: (a) 4.76 mm (3/16 in); (b) 7.94 mm (5/16 in); (c) 12.7 mm (1/2 in); and (d) 15.88 mm (5/8 in). Note that results are reported for wall deformations greater than those needed for the steel plate to attain its plastic moment. As seen in Fig. 15a–d, bearing forces develop at a certain distance from the second tie bar elevation (note that the second tie bar is 305 mm (12 in) above the wall base). Figure 15 also shows that the distributed forces increase in amplitude and act over a greater surface with increasing plate thicknesses, which results in larger values of the prying length and prying forces.

Figure 16a–d shows the build-up of the bearing nodal forces along the half plate width with increasing axial wall deformation. Note that, the distance between the second tie bar elevation [305 mm (12 in)] and the peak points of each of the single curves (at maximum axial deformation) are taken as prying lengths, and they are reported at every 25.4 mm (1 in) along the width of the plate from the wall zero location. The figures also show a uniform buckling wave along the plate width such that the peak amplitudes of the nodal forces (obtained along the plate width) have almost the same values with small variations when M_p is attained. For example, consider the nodal force distribution in Fig. 16d; the peak values of the nodal forces at the maximum axial deformations are about 1.25 kN (0.28 kips). Note that force values obtained at the zero-width

location are almost half the values reported in Fig. 16 due to assignment of the symmetry boundary condition at these nodes and these values should be considered to actually be twice as large compared to the values reported.

As observed from Fig. 16, the prying lengths and the pressure amplitudes increase with the thickness of the plate per equilibrium of moments with the developed plastic moment (recall that, per Eq. (2), $M_p = Q_{max} L_{pr}$). For example, per Fig. 16a–d at the maximum wall deformation, the average values of the prying lengths (reported within each plot) are: 49.8 mm (0.78 in), 61.6 mm (2.425 in), 86.1 mm (3.39 in), and 101.9 mm (4.012 in); and the summed values of the nodal forces are: 11.8 kN (2.65 kip), 26.2 kN (5.89 kip), 50.7 kN (11.4 kip), and 71.3 kN (16.02 kip) for the cases of plate thicknesses equal to $t_s = 4.76$ mm (0.187 in), 7.94 mm (0.313 in), 12.7 mm (0.5 in), and 15.88 mm (0.625 in), respectively.

The variation of prying length (L_{pr}) and corresponding tie bar axial force with plate thickness and tie bar diameter is shown in Fig. 17a–b. Note that, the L_{pr} values reported in Fig. 17a are the average values obtained along the width of the plate reported in Fig. 16a–d; and the tie bar force values reported in Fig. 17b were obtained directly as element forces. As shown in Fig. 17a, the prying length increases (almost linearly) with increasing plate thickness and reduces slightly with larger tie bar diameters. The slight reduction of the L_{pr} values with larger tie bar diameters is attributed to the ability

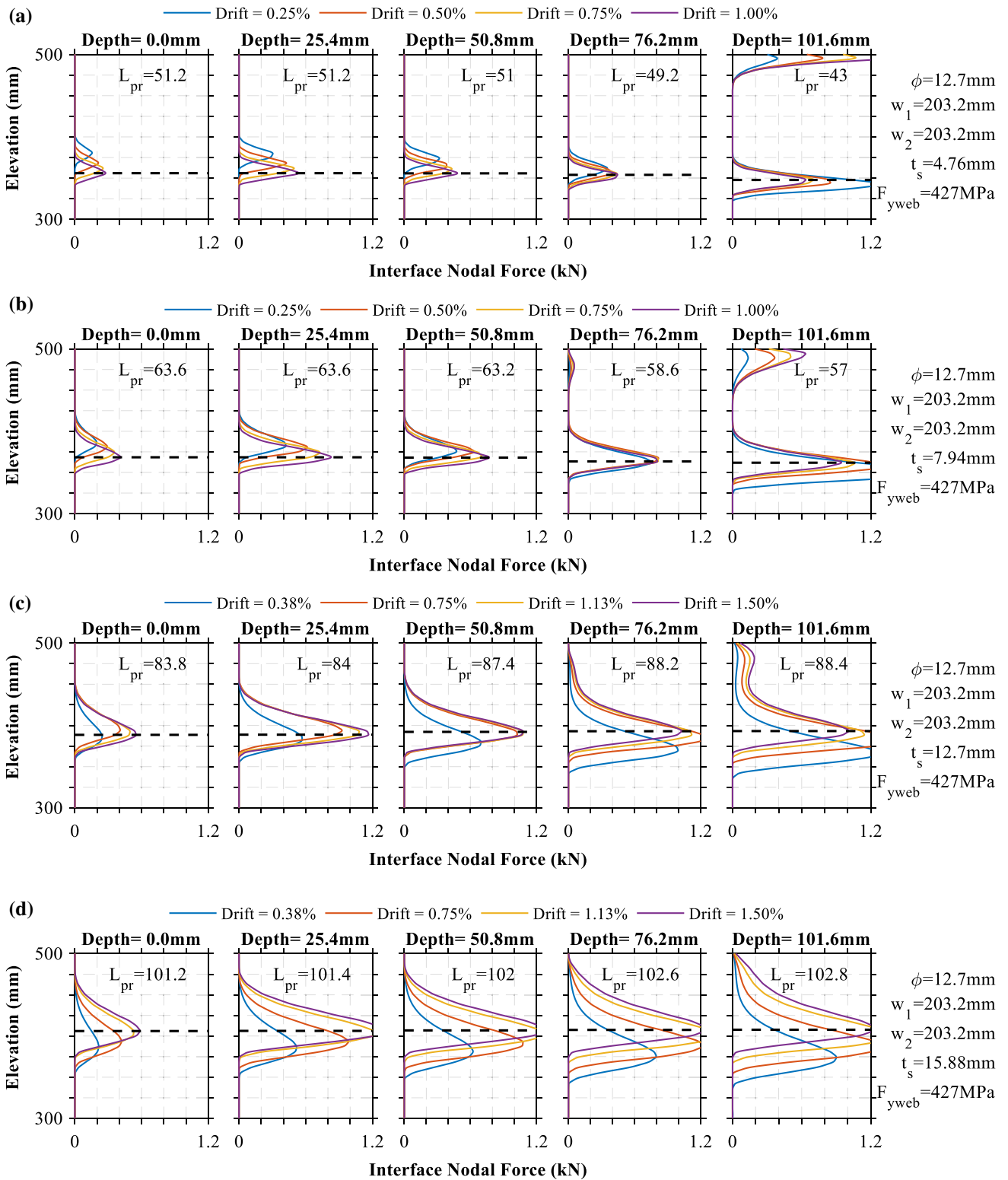
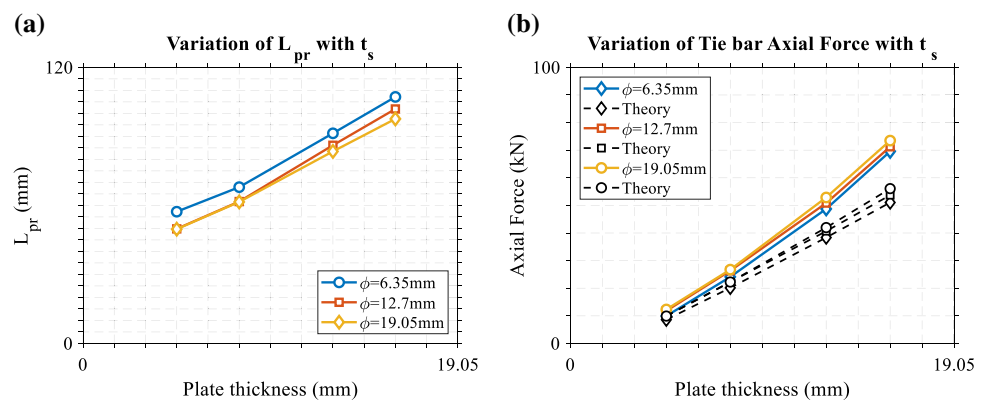


Fig. 16 Distribution of bearing nodal forces due to prying action as a function of axial wall deformation considering plate thicknesses of: **a** 4.76 mm (3/16 in); **b** 7.94 mm (5/16 in); **c** 12.7 mm (1/2 in), and; **d** 15.88 mm (5/8 in)

Fig. 17 Effect of plate thickness: **a** on prying length; **b** on tie bar axial force



of flexurally stiffer tie bars to contribute in resisting some of the plate bending moment. However, the bending stiffness of tie bars is generally small and can be ignored. For example, for the wall with $t_s = 15.88$ mm (5/16 in) and $\phi = 19.05$ mm (0.75 in), the numerically predicted value of the bending moment in the tie bar (at the ultimate drift) is about 158 kN mm (1.4 kip-in), while the bending moment from the plate plastic hinge is 1322 kN mm (11.7 kip-in). For the same wall but with $\phi = 0.5$ in, the bending moment in the tie bar reduces to 45 kN mm (0.4 kip-in). Note that the yield moments of the tie bars are 17.3 kN mm (0.153 kip-in), 138 kN mm (1.221 kip-in), 467 kN mm (4.133 kip-in), for $\phi = 6.35$ mm (0.25 in), 12.7 mm (0.5 in), and 19.05 mm (0.75 in), respectively.

The theoretical results of T_T , computed using Eq. (2), are also shown in Fig. 17b. Note that the numerically obtained average L_{pr} values from Fig. 17a were used for this calculation since there is no closed-form solution available at this time to determine this length, and; the M_p values were computed using Eq. (3). As shown in Fig. 17b, tie bar axial forces increase in the presence of thicker steel plates, and also slightly increase with increasing tie bar diameters. The observed slight increase of forces with increasing tie bars diameters is attributed to the reduced L_{pr} value that is obtained with larger tie bars.

Note that the difference between the theoretical results and the numerically obtained values increases with the plate thickness. This is attributed to the influence of the secondary moment ($P\Delta_1$) in plate bending. The required axial force, P , for thicker plates is higher to obtain the same amount of plate deformation, Δ_1 .

Note that, tie bar axial force demand created by prying action, compared to forces created by the confining action, is relatively small for well-proportioned walls. For example, the previously examined tie bar axial force demand (i.e., for Tie₂₂) for Model A-2 under confining pressures was 143 kN (32 kips) for $t_s = 25.4$ (1 in), where Model A-2 is the one for which buckling was prevented; recall that this is equivalent to $t_s = 7.94$ mm (5/16 in) and $w_2 = 152$ mm (6 in) in Model A where local buckling was not prevented. The tie bar axial

force demand due to prying action, obtained here for the same plate thickness of 7.94 mm (5/16 in) and $w_2 = 203$ mm (8 in) is about 25 kN (5.62 kips). Scaling for the narrower tie bar spacing of $w_2 = 152$ mm (6 in) gives approximately 19 kN (4.27 kips), which is nearly 13% of the tie bar axial force due to confining pressure alone.

As shown by Eqs. (1) and (2), tie bar axial force due to prying action will increase with plate thickness because the plate plastic moment varies as a function of the square of the plate thickness, but the above numbers suggest that prying action will not be the dominant factor defining tie bar axial forces, unless future experiments can demonstrate that confinement pressures developed in C-PSW/CF walls are significantly smaller than predicted by the above numerical analyses.

6 Conclusions

In this study, two factors, namely, confinement effects and prying action during local buckling, were numerically investigated to determine their impact on tie bar axial forces under inelastic in-plane flexural wall response. These effects are currently not considered in the design of C-PSW/CF. A tie bar slip model was developed and integrated in the finite element model for this purpose. The KCC model available in LS-Dyna was considered to investigate various aspects of confinement and tie bar axial force demands. The study showed that;

- Variation of axial stress distribution through the thickness of the infill concrete showed that the effectively confined concrete core is less than the nominal core area. The effectively confined core was shown to be influenced by lateral pressure distribution.
- The steel plate-concrete interface nodal force distribution, which illustrates where confinement pressures acting on the steel plates are more significant, follows a conical shape at the tie bar locations. Peak forces at these locations slightly increase with the horizontal and verti-

cal spacing of the tie bar, while the base area of the conical shape is not significantly affected by tie bar spacing. The magnitude of the resulting forces at these locations is significant and drives the development of axial forces in tie bars. These findings provide insights for the formulation of future theoretical models to calculate tie bar axial forces due to confining pressures.

- Plate local buckling introduces a prying mechanism and results in an increase of tie bar axial force demand. The prying action was shown to be related to the thickness and plastic moment of the wall plate, and prying length. A simple equation was developed to calculate prying forces for a known prying length. Although acting concurrently, in comparison to tie bar axial force demand due to confining pressures, the increase in the tie bar axial force due to prying mechanism (due to plate local buckling) is found to be relatively low for typical range of plate thickness, but might become significant for thicker plates or if confinement effect is later experimentally proven to be less significant than obtained numerically.

It is recognized and important to emphasize that the magnitude of concrete dilation is sensitive to the concrete model used and that the results presented in this study are contingent on the models and assumptions adopted in this limited numerical study. Future research is desirable to investigate other concrete models to capture the above effects and translate them in tie bar axial force demands for any composite wall geometry, and to determine when these forces may have an impact on design. This should include parametric studies comparing multiple concrete models in uniaxial, biaxial, and triaxial case studies, together with results for the C-PSW/CF, to determine the most appropriate concrete model to rigorously capture the impact of dilational effects in this application. However, most importantly, this will require experimental results that can provide validation against analytical results, recognizing that getting experimental results of axial forces acting on tie bars can be difficult in C-PSW/CF. Nonetheless, the findings presented in this exploratory paper are critically informative in guiding the design and instrumentation of such future experimental programs by the broader research community, as they identify the fundamental behaviors at play, as well as location and approximate magnitude of key forces, stresses, and strains that drive this behavior.

Appendix 1: Comparative Study using KCC and CSCM Concrete Models

Selection of Concrete Models

This Appendix presents details of the analyses performed to identify a simple concrete model that can reasonably

predict wall strength and account for confinement effect. Note that in the aforementioned study by Polat and Bruneau (2017), the objective was to replicate the in-plane flexural wall response experimentally obtained by Alzeni and Bruneau (2017), focusing on global response and in particular on capturing the pinching effect observed in the hysteretic response, which was believed to be related to the opening and closing of the concrete cracks, and which was modeled successfully using the Winfrith model. Fig. 18 shows the resulting comparison between the experimental and numerically obtained hysteretic curves using that model. Fig. 19 shows the corresponding resulting axial strain distribution in the steel plate. While the steel plate axial strains were predicted well, the wall compression depth was slightly over-predicted. Although good results were obtained with the Winfrith model, this may not be the best model when the objective is to predict the tie bar axial force demand. This is because, in C-PSW/CF, when the concrete sandwiched between steel web plates is under vertical axial compression

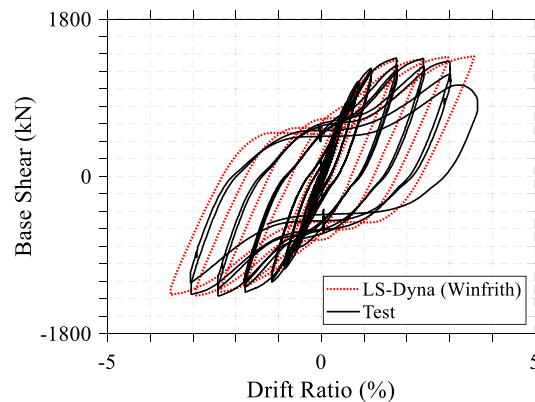


Fig. 18 Comparison of experimental and numerical wall hysteresis using Winfrith model

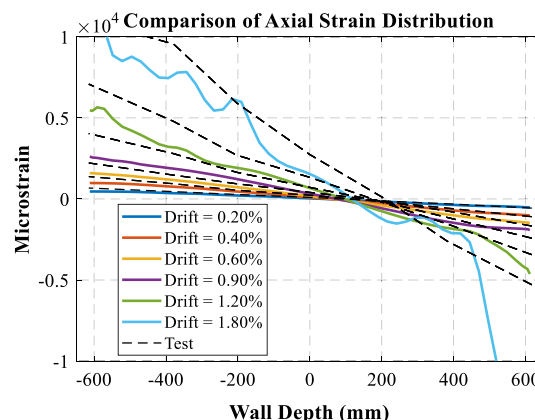


Fig. 19 Comparison of axial strain distribution in steel plate for experimental and numerical resulting using Winfrith model

due to combined bending and axial forces, shear dilation of the concrete can apply a horizontal pressure to the steel plate, which in turn introduces an axial force on the tie bars. This mechanism makes it essential to replicate passive confinement effects due to concrete shear dilation—which, unfortunately, is not a behavior accounted for by the Winfrith model (Wu et al., 2012).

A large number of concrete constitutive models exist that have the ability to model dilation. The KCC and CSCM models were considered here because they offer the option to generate most of the needed model parameters with little user input (although the KCC and CSCM models offer both complex material definition or parameter generation options); as such, structural engineers can easily define the nonlinear behavior of concrete per these models with knowledge of the unconfined uniaxial compressive strength and a few basic concrete properties, namely, mass density for the KCC models, and aggregate size for the CSCM models.

These models have also been investigated by various researchers. In particular, Wu et al. (2012) investigated these concrete models for their effectiveness in capturing key aspects of concrete behavior, namely, post-peak softening, shear dilation, and confinement effects for plain concrete cylinder tests, using LS-Dyna. Schwer and Malvar (2005) compared the results obtained using the KCC model when specifying only the unconfined compression strength of a well characterized 45.6 MPa concrete, based on original well-characterized concrete, with those from various material characterization tests. They reported that the complex behavior of concrete can be modeled successfully with the default parameter generation data of the KCC model. Teranova et al. (2018) used the KCC and CSCM models to generate benchmark stress–strain data using the Smooth Particle Hydrodynamics (SPH) formulation in LS-Dyna. In light of the lack of experimental data on tie bar axial forces in C-PSW/CF, the use of more complex model was also justified at this time.

Description of the Finite Element Modeling

Aspects of the finite element modeling and analysis procedures developed for the reference wall studied by Polat and Bruneau (2017) are described below, as many of these parameters are re-used here. The concrete was modeled using an eight-node solid elements (Solid 1) with reduced integration and hourglass control; the steel web plates and the boundary elements were modeled using four-node fully integrated shell elements (Shell 16), and; tie bars were modeled using two node beam elements with the Hughes-Liu beam formulation (Beam 1) with two integration points. For the steel–concrete interface, the *automatic_surface_to_surface_mortar* contact with an interface friction coefficient of 0.3 was used. The dimensions

of the shell and solid elements were determined based on results from a convergence study. The shell elements were 25.4 mm × 25.4 mm (1 in × 1 in) and the solid elements were 25.4 mm × 25.4 mm × 25.4 mm (1 in × 1 in × 1 in) in size. Note that a total of four layers of concrete in the transverse direction were used in the numerical model of the reference wall.

MAT003 (with kinematic hardening) was used for the steel web plates, half-HSS boundary elements, and tie bars. Note that MAT003 is a bi-linear model which requires the definition of the elastic modulus, E_s , the yield strength, F_y , the tangent modulus, E_T , and a hardening parameter for kinematic hardening or isotropic hardening. The elastic modulus used for the steel web was $E_s = 205,463$ MPa (29,800 ksi) and for the boundary element $E_s = 189,605$ MPa (27,500 ksi), based on experimental results of steel coupons for the specimens. The yield strength used for the steel web was 427 MPa (62 ksi) and for the boundary element 317 MPa (46 ksi). Tangent modulus used for the web plate was 551 MPa (80 ksi) and for the boundary elements 344 MPa (50 ksi). Concrete compressive strength was set as $f'_c = 47.6$ MPa (6900 psi). In the LS-Dyna model, a concrete tensile strength of $f'_t = 4.76$ MPa (690 psi) and a Poisson's ratio, ν , of 0.2 were also specified. For the CSCM concrete model, the unconfined compression strength is 30 MPa (4.351 ksi) (Murray, 2007). Note that for the KCC and CSCM concrete models, the user has the option of directly inputting material properties or requesting default material properties based on the unconfined compressive strength of concrete—as mentioned previously. Note also that, for the default option in the CSCM concrete, the internally calculated values for a number of parameters by the model are reported to have been derived based on the properties of concrete ranging in strength from 20 to 58 MPa (2.901 to 8.412 ksi) (LSTC, 2013; Murray, 2007). In all cases, aggregate size was specified as 7.9 mm (0.31 in.).

The elastic modulus of the concrete, in the benchmarked model, was adjusted to $0.5E_c$ (MPa or ksi) where E_c (psi) = $57000\sqrt{f'_c}$ (psi) to match the experimentally measured wall elastic stiffness. For the KCC model, the elastic modulus of concrete is internally calculated. The value of the internally calculated value for the KCC model can be obtained by checking the output log files from the analysis, which, in this case, confirmed that the values of the elastic modulus was equal to E_c for the wall with the KCC model.

The walls were subjected to in-plane lateral displacements at their top end, applied to all the steel and concrete nodes at that height. The experimental loading protocol provided by (Alzeni & Bruneau, 2017) was used in the numerical solution—details on this protocol are not provided here due to space concerns.

Comparison of Inelastic Cyclic Wall Response Using KCC and CSCM Concrete

Wall response using the KCC and CSCM models were compared against that of the benchmark wall using the Winfrith model, using fixed-based boundary conditions in all cases. Note that the benchmarked wall was originally developed by explicitly accounting for foundation flexibility of the specimens, but this was avoided here because it was unnecessary. Comparison of the resulting hysteretic responses in terms of base moment versus wall drift ratio is shown in Fig. 20a–b, where the results are compared for the walls with: (a) Winfrith and KCC models, and; (b) Winfrith and CSCM models. Note that the wall with the CSCM model exhibits almost no pinching, whereas the amount of pinching captured by the wall with KCC model is somewhat between what has been obtained for the walls with the Winfrith and CSCM models. The prediction of maximum wall strength by the KCC model is almost the same as that for the Winfrith model, whereas, for the CSCM model, it is 9% higher than for the Winfrith model at a 2% drift ratio. Given that confinement is related to wall strength, and that tie bar demands are affected by confinement pressures, the KCC model was deemed to be more adequate for the investigation presented in the main body of the paper, in spite of its shortcoming in capturing global hysteretic response.

Comparison of Confinement Through Concrete Axial Stress Distribution Through Wall Thickness

Fig. 21a–c shows the axial stress distribution in the steel and the concrete obtained from static inelastic pushover analyses along half the wall depth under compression, but excluding the half-HSS ends of the wall. In this figure, the zero position corresponds to the center of the wall and the dotted lines in these figures represent the tie bar locations. Note that, here, the wall thickness is represented as layers equal to the concrete finite element mesh segments through the thickness. Layer 1 corresponds to the outermost layer and Layer 4 corresponds to the innermost layer at the center

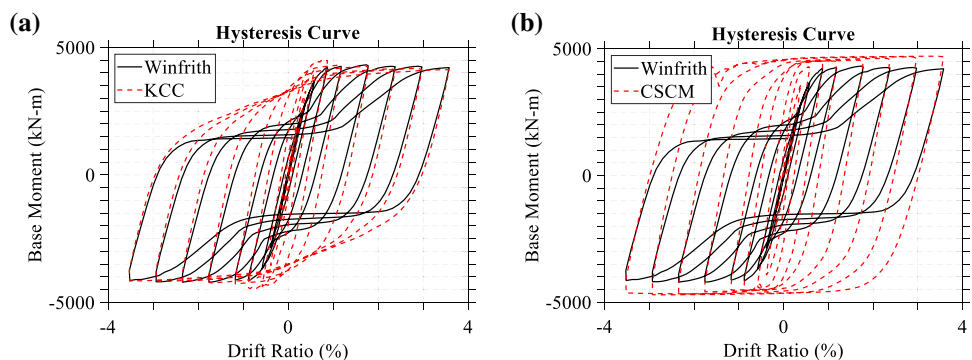
of the concrete wall. For each model, concrete stresses are reported for each layer to observe the variation of confinement through the thickness. The stresses are reported at the wall elevation corresponding to half the distance between the first and second row of tie bars [= 203 mm (8 in)] from the base.

As shown in Fig. 21a for the wall with the Winfrith model, the compression axial stress distribution through the layers of the infill concrete does not change significantly. Moreover, all the concrete layers exhibit a stress block with a peak strength of approximately 60 MPa (8.7 ksi). This gives the wall a minor increase in flexural strength considering the unconfined strength of 48 MPa (6.9 ksi). This indicates that some confinement is provided by the pressures developed in the boundary elements. The consequence of web plate buckling is also visible, as expressed by the progressive reduction of axial stresses resisted by the steel plate, most significantly observed at 3% and 4% drift.

As shown in Fig. 21b for the wall with the KCC model, the compression axial stress distribution varies through the thickness with higher values at the innermost layers than at the outermost ones—this is attributed to the model's ability to simulate shear dilation and hence capture confinement effects. Note that the maximum compressive stresses reached at mid-layer is more than double the values measured for the wall with the Winfrith model. For example, the peak strength is about 150 MPa (21.8 ksi) in Layer 4 (compared to 60 MPa (8.7 ksi) in the wall with the Winfrith model). For the wall with the KCC model, the compression depth is approximately 100 mm (3.94 in) less than for the wall with the Winfrith model.

As shown in Fig. 21c for the wall with the CSCM model, the compression axial stress distribution also varies through the thickness as a consequence of concrete shear dilation. The maximum compressive stress reached at mid-thickness of the wall is about 75 MPa (10.9 ksi). Note that, the compression depth is increased by as much as 75 mm (2.95 in) compared to the wall with the Winfrith model. For this wall, the axial stress distribution of the steel plate indicates significant plate buckling.

Fig. 20 Comparison of cyclic in-elastic base moment hysteresis: **a** Winfrith and KCC, and; **b** Winfrith and CSCM



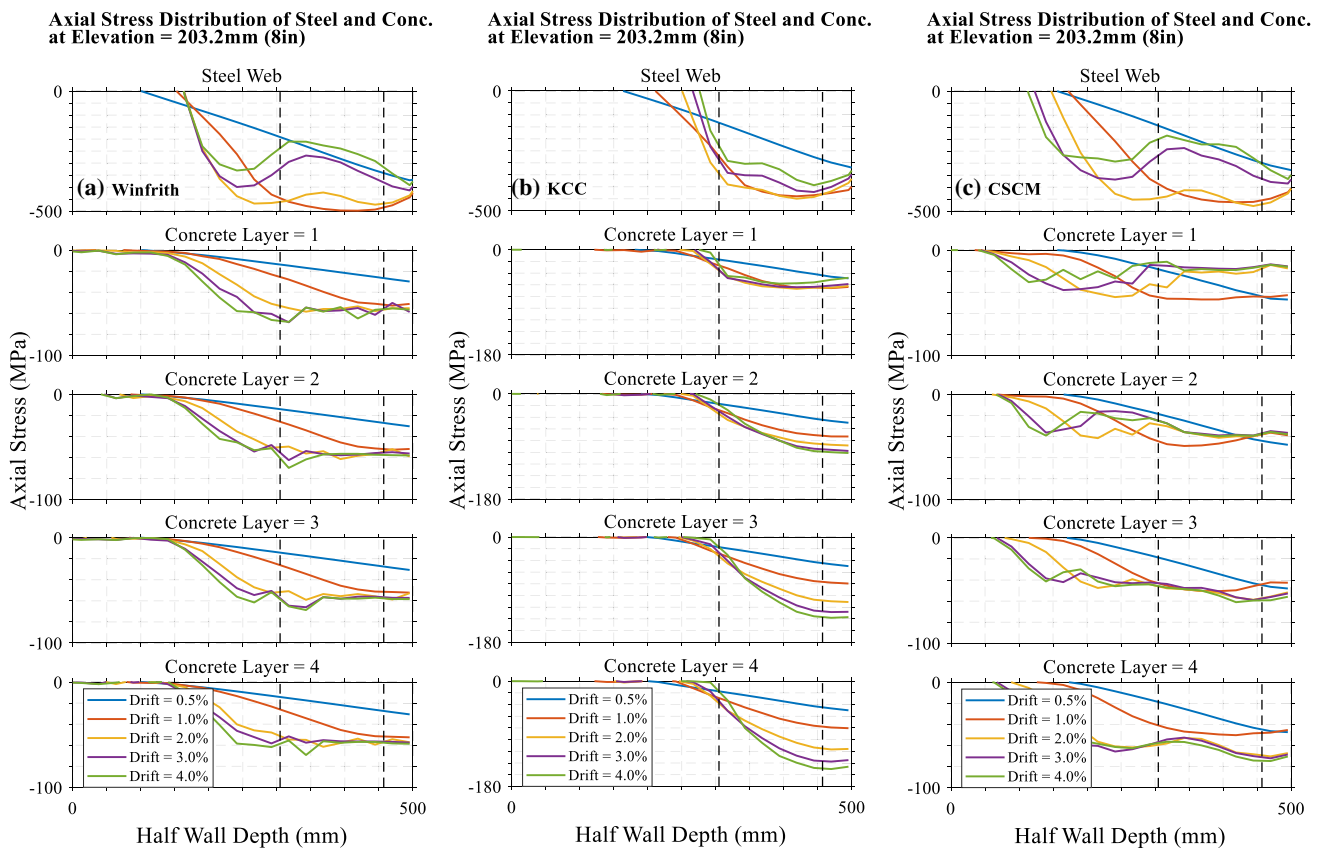


Fig. 21 Axial stress distribution in steel and concrete along half wall depth from FE models with concrete models: **a** Winfrith, **b** KCC, and; **c** CSCM (vertical dotted lines denote tie locations)

Comparison of Tie Bars Axial Force Demand

Here, axial force response of tie bars obtained from the static inelastic pushover analyses are compared. Fig. 22a–c shows the axial force demands for the four tie bars identified in Fig. 1b. As shown in Fig. 22a, relatively low axial forces are obtained when using the Winfrith model compared to the ones using the KCC (Fig. 22b) and the CSCM (Fig. 22c)

models. Larger tie bar forces are created when using the KCC and CSCM models, evidently due to the ability of these models to account for shear dilation. For example, for Tie₂₂, axial demands obtained at 4% drift are 6 kN (1.4 kips), 120 kN (27 kips), and 59 kN (13.3 kips) for the walls with the Winfrith, KCC and CSCM models, respectively. Results indicate that, in this case, tie bars remain elastic for all cases. Assuming a 345 MPa (50 ksi) yield strength of tie

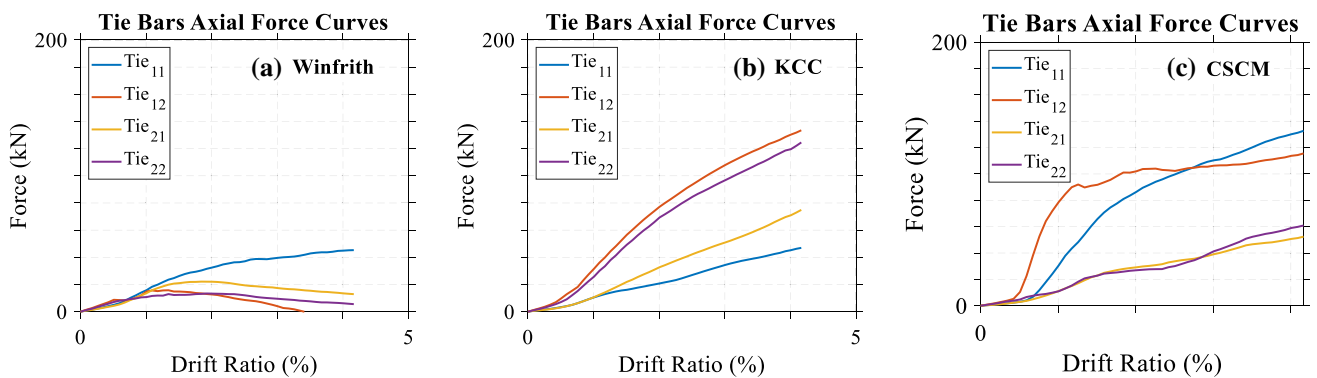


Fig. 22 Axial force of tie bars of the walls with concrete material models of: **a** Winfrith; **b** KCC, and; **c** CSCM

bars and a 25.4 mm (1 in) bar diameter, the yield capacity of a tie bar is 175 kN (39.3 kips). Note that maximum force demand occurs in different tie bars for each model. For the wall with the Winfrith and CSCM models, maximum tie bar force occurs in Tie₁₁ (interior tie bar), whereas it occurs in Tie₁₂ (exterior tie bar) for the wall with the KCC material model. This is attributed to differences in the width of the concrete compressive stress blocks—previously shown in Fig. 21—which is closer to interior tie bars (e.g., Tie₁₁ and Tie₁₂) for the walls with the Winfrith and CSCM models, and closer to exterior tie bars (e.g., Tie₂₁ and Tie₂₂) for the wall with the KCC model.

Summary of Findings on Selection of Concrete Model

For the work presented study, various aspects of wall behavior were compared to select a concrete model that is able to provide an acceptable representation of global wall response while at the same time allowing to consider concrete confinement and associated tie bars axial force responses. For this purpose, inelastic cyclic wall responses obtained using the KCC and CSCM models were first compared with the previously benchmarked wall response (from prior research) using the Winfrith concrete. Then, concrete confinement behavior was investigated for the three concrete models by plotting and comparing the concrete axial stress distributions across the wall depth and concrete thickness. Finally, tie bars axial force responses were investigated for the three concrete models by plotting and comparing axial forces for a certain set of tie bars. On the basis of this work, it was determined, as described in Sect. 3.2, that while both the KCC and CSCM models could not simulate the pinching experimentally observed in the inelastic hysteretic flexural behavior of the walls, results from the wall using KCC model was better in agreement with the actual wall response. Likewise, with respect to axial stress distribution along the cross-section, compression depth obtained with KCC model was found to be in better agreement with experimental results. Consequently, of the three models considered, the KCC model was retained for the exploratory work presented in this paper.

Funding The financial support for the first author was provided by Scientific and Technological Research Counsel of Turkey for his post-doctoral work at the State University of New York at Buffalo, NY. This support is gratefully acknowledged. However, any opinions, findings, conclusions, and recommendations presented in this paper are those of the writers and do not necessarily reflect the view of the sponsors.

Declarations

Conflicts of interest Not applicable.

References

- AISC. (2016). Seismic provisions for structural steel buildings. *AISC 341-16*. American Institute of Steel Construction, Chicago, IL.
- AISC. (2022). Seismic provisions for structural steel buildings (public review document—available online August 2020). *AISC 341-22*. American Institute of Steel Construction, Chicago, IL.
- Alzeni, Y., & Bruneau, M. (2014). Cyclic inelastic behavior of concrete filled sandwich panel walls subjected to in plane flexure. *Technical Report MCEER, 14-009*, Univ. at Buffalo, the State Univ. of New York, Buffalo, NY, MCEER.
- Alzeni, Y., & Bruneau, M. (2017). In-plane cyclic testing of concrete-filled sandwich steel panel walls with and without boundary elements. *Journal of Structural Engineering, 143*(9), 04017115.
- Bhardwaj, S. R., Varma, A. H., & Orbovic, N. (2019). Behavior of steel-plate composite wall piers under biaxial loading. *Journal of Structural Engineering, 145*(2), 04018252.
- Bruneau, M., Kenarangi, H., & Murphy, T. P. (2018). *Contribution of steel casing to single shaft foundation structural resistance*. NCHRP Research Report 872. Washington, DC: Transportation Research Board.
- Corus, U. (2003). *Bi-steel design and construction guide*. . Corus UK Ltd.
- Epacakchi, S., Whittaker, A. S., Varma, A. H., & Kurt, E. G. (2015). Finite element modeling of steel-plate concrete composite wall piers. *Engineering Structures, 100*, 369–384.
- Hibbett, K., & Sorensen. (2011). *ABAQUS/standard: User's manual*. Dassault Systèmes Simulia.
- Imani, R., & Bruneau, M. (2014). Post-earthquake fire resistance of ductile concrete filled double-skin tube columns. *Technical Report MCEER, 14-0008*, Univ. at Buffalo, the State Univ. of New York
- Kurt, E. G., Varma, A. H., Booth, P., & Whittaker, A. S. (2016). In-plane behavior and design of rectangular sc wall piers without boundary elements. *Journal of Structural Engineering, 142*, 04016026.
- LSTC. (2013). *Keyword User's Manual*. (Vol. II). Livermore Software Technology Corporation (LSTC), Livermore, CA, USA.
- Mazzoni, S., McKenna, F., Scott, M. H., & Fenves, G. L. (2006). OpenSees command language manual. *Pacific Earthquake Engineering Research (PEER) Center*, 264.
- Murray, Y. D. (2007). Users manual for LS-DYNA concrete material model 159. Federal Highway Administration.
- Polat, E., & Bruneau, M. (2017). Modeling cyclic inelastic in-plane flexural behavior of concrete filled sandwich steel panel walls. *Engineering Structures, 148*, 63–80.
- Polat, E., & Bruneau, M. (2018). Cyclic inelastic in-plane flexural behavior of concrete filled sandwich steel panel walls with different cross-section properties. *Engineering Journal, American Institute of Steel Construction, 55*, 45–76.
- Ramesh, S. (2013). Behavior and design of earthquake-resistant dual-plate composite shear wall systems. Purdue University.
- Schwer, L. E., & Malvar, L. J. (2005). Simplified concrete modeling with* MAT_CONCRETE_DAMAGE_REL3. *JRI LS-Dyna User Week*, 49–60.
- Terranova, B., Bhardwaj, S., Whittaker, A., Varma, A., & Orbovic, N. (2019). An experimental investigation of the effects of out-of-plane loading on the in-plane seismic response of SC wall piers. *Engineering Structures, 190*, 380–388.
- Terranova, B., Whittaker, A., & Schwer, L. Benchmarking concrete material models using the SPH formulation in LS-DYNA. In *Proceedings, 15th international LS-DYNA users conference, Dearborn, MI, June*
- Terranova, B., Whittaker, A. S., Epacakchi, S., & Orbovic, N. (2017). Response of steel-plate concrete (SC) wall piers to combined in-plane and out-of-plane seismic loadings. *Technical report*

- MCEER, 17-0003, Univ. at Buffalo, the State Univ. of New York, Buffalo, NY, MCEER.
- Varma, A. H., Malushte, S. R., Sener, K. C., & Lai, Z. (2014). Steel-plate composite (SC) walls for safety related nuclear facilities: design for in-plane forces and out-of-plane moments. *Nuclear Engineering and Design*, 269, 240–249.
- Varma, A. H., Shafaei, S., & Klemencic, R. (2019). Steel modules of composite plate shear walls: Behavior, stability, and design. *Thin-Walled Structures Thin-Walled Structures*, 145, 106384.
- Wu, Y., Crawford, J. E., & Magallanes, J. M. Performance of LS-DYNA concrete constitutive models. In *Proceedings 12th international LS-DYNA users conference* (pp. 3–5).
- Zhang, K., Varma, A. H., Malushte, S. R., & Gallocher, S. (2014). Effect of shear connectors on local buckling and composite action in steel concrete composite walls. *Nuclear Engineering and Design*, 269, 231–239.

Publisher's Note Springer Nature remains neutral with regard to jurisdictional claims in published maps and institutional affiliations.